JGR Space Physics

RESEARCH ARTICLE
10.1029/2023JA032277

Absence of High Frequency Echoes From Ionosondes During the 23–25 April 2023 Geomagnetic Storm; What Happened?

John Bosco Habarulema[1,2,3], Yongliang Zhang[4], Tshimangadzo Matamba[1], Dalia Buresova[5], Gang Lu[6], Zama Katamzi-Joseph[1,2], Paulo Roberto Fagundes[7], Daniel Okoh[8,9], and Gopi Seemala[10]

[1]South African National Space Agency (SANSA), Hermanus, South Africa, [2]Department of Physics and Electronics, Rhodes University, Makhanda, South Africa, [3]Centre for Space Research, Physics Department, North-West University, Potchefstroom, South Africa, [4]Johns Hopkins University Applied Physics Laboratory, Laurel, MD, USA, [5]Institute of Atmospheric Physics, Prague, Czech Republic, [6]High Altitude Observatory, National Center for Atmospheric Research 3080 Center Green Drive, Boulder, CO, USA, [7]Laboratório de Física e Astronomia, Universidade do Vale do Paraíba (UNIVAP), São José Dos Campos SP, Brazil, [8]United Nations African Regional Centre for Space Science and Technology Education - English, UN-ARCSSTE-E, Obafemi Awolowo University Campus, Ile Ife, Nigeria, [9]Istituto Nazionale Geofisica e Vulcanologia (INGV), Roma, Italy, [10]Indian Institute of Geomagnetism, Mumbai, India

Key Points:

- HF signals were not reflected back to the ionosonde location during part of the main phase possibly due to ionospheric tilting
- Maximum electron density of the F2 layer derived from GNSS observations correctly identify the negative ionospheric storm effect
- The auroral oval moved closer to mid latitudes during the storm main phase

Supporting Information:

Supporting Information may be found in the online version of this article.

Correspondence to:

J. B. Habarulema,
jhabarulema@sansa.org.za

Citation:

Habarulema, J. B., Zhang, Y., Matamba, T., Buresova, D., Lu, G., Katamzi-Joseph, Z., et al. (2024). Absence of high frequency echoes from ionosondes during the 23–25 April 2023 geomagnetic storm; what happened? *Journal of Geophysical Research: Space Physics*, *129*, e2023JA032277. https://doi.org/10.1029/2023JA032277

Received 15 NOV 2023
Accepted 5 MAR 2024

Abstract We report an unusual event on absence of high frequency (HF) echoes in ionosonde observations from the ionospheric F2 region during the geomagnetic storm of 23–25 April 2023. This event was observed in both southern and northern hemispheres over two stations, Grahamstown (33.3°S, 26.5°E), South Africa and Pruhonice (50.0°N, 14.6°E), Czech Republic. Significant O/N_2 depletion over the stations was observed by TIMED/GUVI, indicating a strong negative ionospheric storm. This is unique since absence of echoes in ionosonde measurements is usually due to strong radio absorption in the ionosphere associated with solar flares. However, there was no flare activity during the periods of "absent" F2 HF echoes. On the other hand, the ionosonde detected echoes from E-layer. TIEGCM simulation reproduced TIMED/GUVI O/N_2 depletion and showed that NmE was larger than NmF2 on dayside over Pruhonice. TIMED/GUVI O/N_2 also showed a clear spatial gradient in the O/N_2 depleted regions, suggesting F-region ionosphere was tilted. By estimating the critical frequency of the F2 layer using GNSS observations, we have shown that it wasn't possible for the ionospheric electron density to reach depletion levels prohibiting reflection of HF echoes from ionosondes. We suggest that this phenomena may have been caused by either (a) maximum electron density of E layer exceeding that of F2 layer and/or (b) ionospheric tilting which made the signals to be reflected far away from the ionosonde locations.

Plain Language Summary Solar eruptions such as coronal mass ejections (CMEs) can lead to geomagnetic storms which cause temporal disturbances in the Earth's thermospheric temperature and composition as well as profound changes in ionospheric electron densities. One of the consequences for this phenomena is the negative ionospheric storm where ionospheric electron density is reduced from its "regular" background values. In this study, we report on the temporal absence of high frequency (HF) radio echoes from the ionospheric F2 layer in ionosonde measurements during the geomagnetic storm of 23–25 April 2023. Thermospheric neutral composition observations and simulation suggested that the absence of HF echoes was due to the intense negative ionospheric storm.

1. Introduction

Geomagnetic storms are among the prominent consequences of effective solar wind–magnetosphere–ionosphere coupling which largely determine the amount of energy input into the ionosphere during the "short-lived (about 2–7 days)" temporal disturbance of the Earth's magnetic field. In the ionosphere, geomagnetic storms lead to a range of dynamic and electrodynamic processes which modify the background electron density at different time scales in high, mid and equatorial latitude regions (e.g., Fuller-Rowell et al., 1996; Danilov, 2001; Tsurutani et al., 2004; Prölss & Jung, 1978). The mostly reported ionospheric influences as a result of geomagnetic storms are positive and negative storm effects simply refering to increase and decrease in ionospheric electron density (e.g., in the F2 region), respectively (e.g., Fuller-Rowell et al., 1996; Danilov, 2001). Both these effects can have their origin in either dynamic or electrodynamic mechanisms and in some cases, both could have a simultaneous role to play. The general accepted

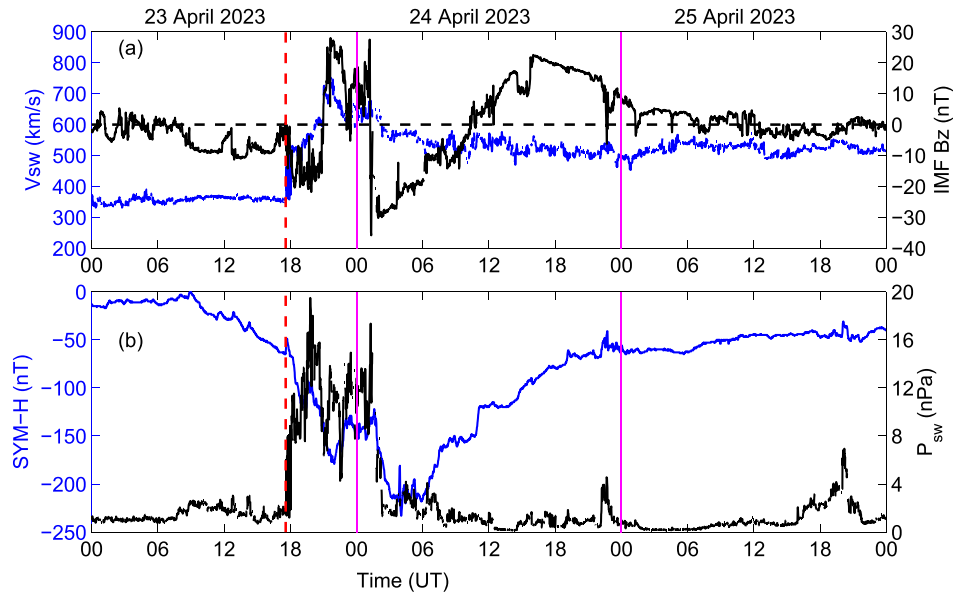

Figure 1. Changes in (a) solar wind velocity, V_{sw} (blue curve) and interplanetary magnetic field, IMF Bz (black curve); (b) SYM-H (blue curve) and solar wind dynamic pressure, P_{sw} (black curve) for 23–25 April 2023.

mechanism for negative storm effects is the change in thermospheric composition which may be quantified using the variability in Oxygen to molecular Nitrogen (O/N_2) ratio (Burns et al., 1995; Zhang et al., 2004). This is the prevalent behaviour caused by storms in summer hemisphere (e.g., Fuller-Rowell et al., 1994, 1996). Penetrating electric fields of magnetospheric origin which usually occur during the southward turning of IMF Bz cause simultaneous increase in electron density at all latitudes (e.g., Tsurutani et al., 2004; Danilov, 2001) and further contributes to the expansion of equatorial ionization anomaly towards midlatitude especially during local daytime (Huang, 2012; Tsurutani et al., 2004). Ionospheric effects related to disturbed ionospheric dynamo have delayed response time, for example, in mid and low latitudes as they involve the induced storm time thermospheric winds influencing the atmosphere's electrical conductivity along magnetic field lines (e.g., Blanc & Richmond, 1980). There are other dynamic processes such as atmospheric gravity waves which result into traveling ionospheric disturbances that can be observed at different latitude regions and are partly responsible for positive storm effects (e.g., Prölss & Jung, 1978). In this paper, we focus on the two stage geomagnetic storm period of 23–25 April 2023 which exhibited two minima SYM-H values of −179 nT (2159 UT) and −233 nT (0403 UT) on 23 and 24 April 2023, respectively. While the predominant ionospheric response at midlatitudes of both northern and southern hemispheres over the African-European sector was a negative storm effect that coincided well with a significant decrease in O/N_2 ratio, we zoom in into the absence of returned echoes in ionosonde measurements (an observation mostly seen for the F2 region) during part of the storm main phase on 24 April 2023. We note that there were no solar flare activity to explain this phenomena, which makes it interesting to investigate in details.

2. Data Sources and Methods

2.1. Solar Wind and Geophysical Conditions

The geomagnetic storm of 23–25 April 2023 was associated with the interplanetary coronal mass ejection (ICME) whose shock front was observed at L1 on 23 April 2023 at 17:00 LT (Ghag et al., 2023). The shock hit the Earth's magnetosphere 45 min later at 17:45 UT on 23 April 2023 triggering a geomagnetic storm. To show the storm evolution, we display three solar wind parameters namely; solar wind velocity, the Bz component of the interplanetary magnetic field (IMF Bz) and solar wind dynamic pressure (P_{sw}) obtained from the OMNI database (https://spdf.gsfc.nasa.gov/pub/data/omni/high_res_omni/). The strength of the equatorial ring current and hence geomagnetic storm is provided by the SYM-H (nT). Figure 1 shows V_{sw} (blue curve) and IMF Bz (black curve) in panel (a) while P_{sw} (nPa) and SYM-H (nT) are plotted in (b).

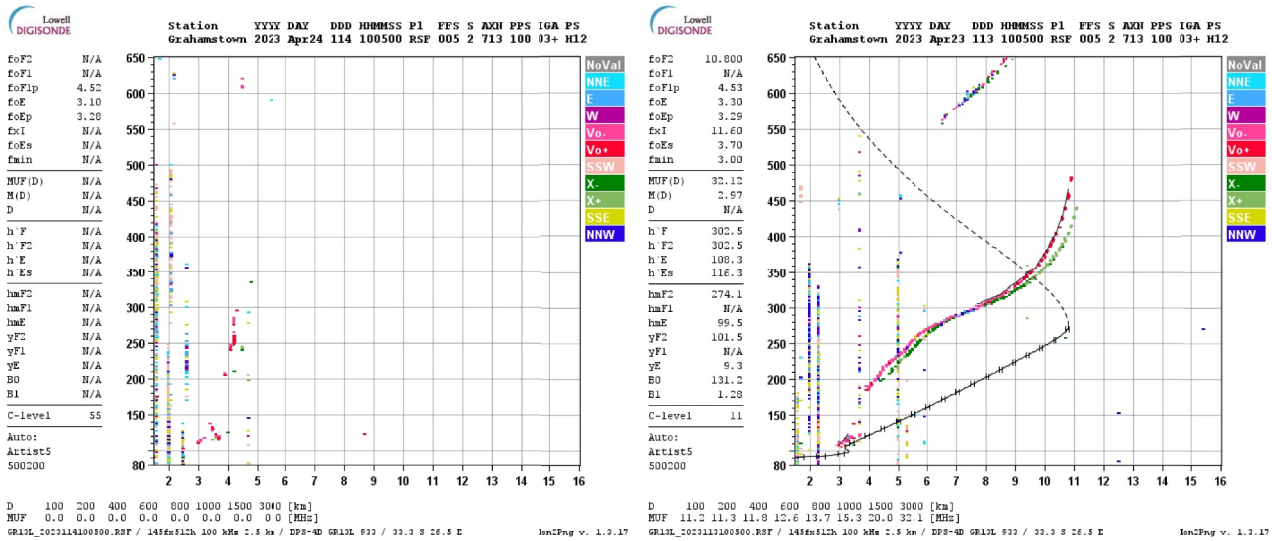

(a) Ionograms over Grahamstown (33.3°S, 26.5°E) on 24 (left) and 23 (right) April 2023 at 1005 UT.

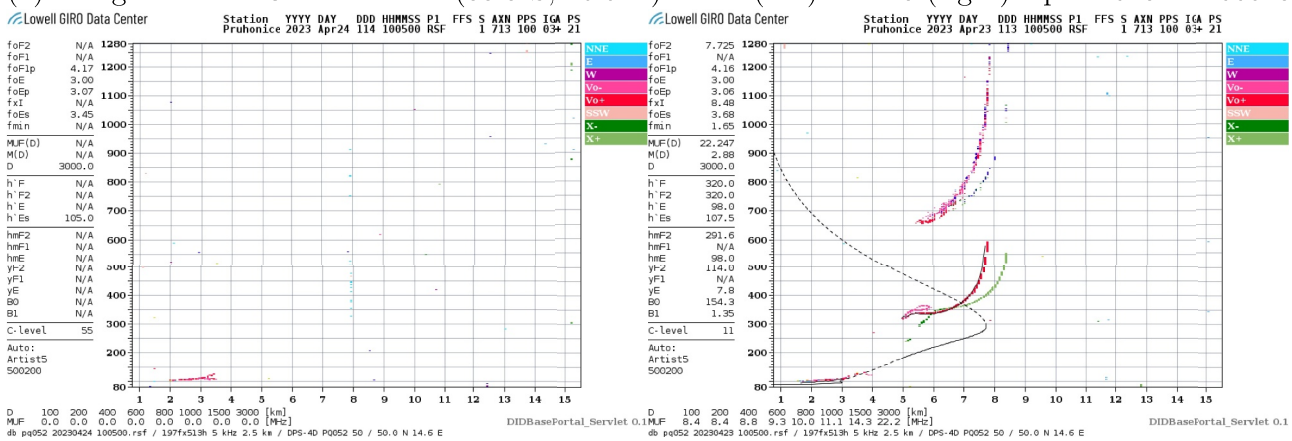

(b) Ionograms over Pruhonice (50.0°N, 14.6°E) on 24 (left) and 23 (right) April 2023 at 1005 UT.

Figure 2. Ionograms over Grahamstown, GR13L (33.3°S, 26.5°E) and Pruhonice, PQ052 (50.0°N, 14.6°E) on 24 (left) and 23 (right) April 2023 at 1005 UT.

In Figure 1a, the storm commenced at 17:45 UT (shown by a red vertical dashed line) with V_{sw} abruptly increasing from around 350 km/s to 500 km/s on 23 April 2023. IMF Bz fluctuated between 0 nT (at storm onset) and −20 nT for about 2–3 hr. The SYM-H data shows what has been described as a two-step geomagnetic storm (Ghag et al., 2023), with SYM-H minima values of −179 nT (2159 UT) and −233 nT (0403 UT) on 23 and 24 April 2023, respectively. Maxima V_{sw} and P_{sw} values of about 750 km/s (2139 UT) and 19.5 nPa (1949 UT) were reached on 23 April 2023.

2.2. Ionosonde and GPS Observations

Absence of HF echoes especially from the F2 region during the geomagnetic storm were observed using ionosonde data from Grahamstown, GR13L (33.3°S, 26.5°E), South Africa and Pruhonice, PQ052 (50.0°N, 14.6°E), Czech Republic. On the 24 April 2023, extremely faint or no F2 region echoes at all were evident during 0255–0440 UT, 0950–1025 UT and thereafter intermittently until 1140 UT over GR13L; as well as for PQ052 during 0830–1130 UT. Very clear ionograms over GR13L recovered at around 1145 UT. Figure 2 shows examples of ionograms during the times when there were no clear echoes on 24 April 2023 over GR13L and PQ052. The left

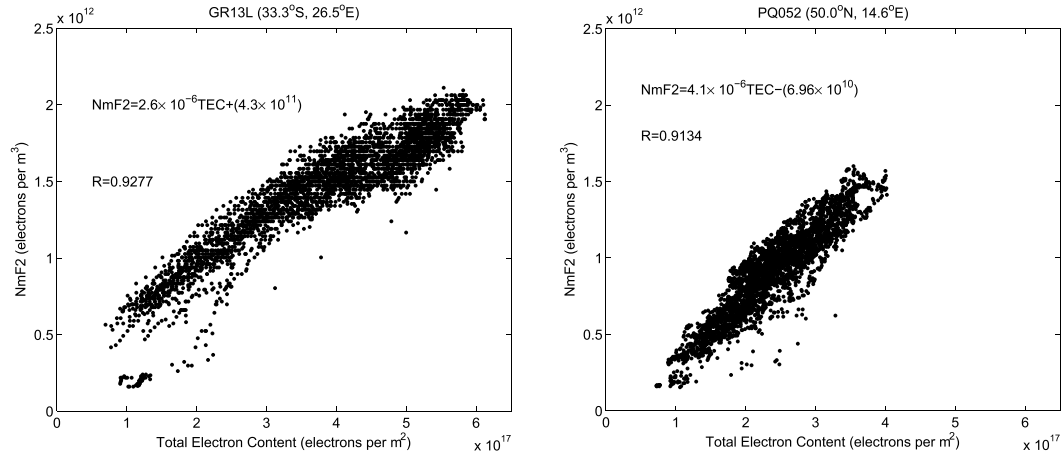

Figure 3. Relationship between maximum electron density at F2 layer (NmF2) and total electron content (TEC) over GR13L and PQ052 during local daytime (07–18 LT) for April 2023.

panels of Figures 2a and 2b show ionograms over GR13L and PQ052 on 24 April 2023 at 1005 UT. This is equivalent to 1151 and 1103 local time over GR13L and PQ052, respectively when the F2 layer is expected to be fully developed as seen in the right panels of the figure at exactly the same time on 23 April 2023, a day at a time before the commencement of the geomagnetic storm. Movies of ionograms for 24 April 2023 over GR13L and PQ052 are shown in Supporting Information S1.

Usually, absence of HF echoes during local daytime happens during periods of solar flare activity (e.g., Mitra, 1974; Yasyukevich et al., 2018; Fagundes et al., 2020). However, there were no flares during this time period. The resulting question then becomes: what happened? The first suspicion was that the ionospheric electron density could have been depleted to extreme levels insufficient enough to reflect radio waves in HF band. To investigate whether this can be possible, we estimated maximum electron density values of the F2 layer (NmF2) using total electron content (TEC) data derived from GPS observations. Due to the presence of significant night time plasmaspheric contribution within GPS TEC (e.g., Yizengaw et al., 2008; Habarulema et al., 2021, and references therein), we apply the direct relationship between NmF2 (foF2) and TEC only during local daytime (0700–1800 LT). The estimation of foF2 from TEC is mainly based on their linear relationship with correlation values reaching 0.8 and above (e.g., Kouris et al., 2004; Ssessanga et al., 2014). In the integration process while deriving TEC, the value that contributes most is NmF2 (e.g., Ssessanga et al., 2014) which is directly proportional to the square of foF2 (e.g., McNamara, 1991). Thus, foF2 can be derived from TEC or vice versa when their colocated measurements are available based on their simple mathematical relationship especially during local daytime. After estimating foF2 from GPS TEC, we compare the results with monthly median maximum critical frequency of the E layer (foE). Based on the observation capabilities of the ionosonde instrument, for electron density to be depleted enough not to reflect radio waves, such densities should be below the E-region densities which are estimated based on monthly median values. Figure 3 shows scatter plots of NmF2 and TEC over GR13L and PQ052 for April 2023 during 0700–1800 LT. While the ionosonde and GPS receiver are co-located over GR13L, the closest available GPS receiver to PQ052 is Ondrejov, GOPE (49.9°N, 14.8°E) translating into 18 km separation which is insignificant given that the ionospheric correlation distance even during geomagnetic storms can exceed 500 km in midlatitude regions.

We have opted to derive the linear relationship and correlation values based on NmF2 and TEC with their full units instead of foF2 and TEC as is usually done in order to compare similar units. This has previously shown to provide better results (Pignalberi et al., 2019). For example, the correlation value increased from 0.8948 (for foF2 (MHz) and TEC (TECU)) to 0.9235 over GR13L for April 2023 (0700–1800 LT) when NmF2 (electrons per m^3) and TEC (electrons per m^2) were used. TEC is derived using an algorithm that assumes the ionosphere as thin layer at an altitude of 350 km (Seemala, 2023). In the analysis, the elevation threshold used to minimize multipath errors was set to 20°. Details about the TEC derivation software can be found in Seemala (2023). After estimating

NmF2 from TEC data for 23–25 April 2023 using equations displayed in Figure 3, foF2 is calculated using the well established formulation (e.g., McNamara, 1991)

$$foF2 = \sqrt{\frac{NmF2}{1.24 \times 10^{10}}} \quad (1)$$

where foF2 and NmF2 are the critical frequency and maximum electron density of the F2 layer in MHz and electrons per m^3, respectively.

We have also utilized TEC data to investigate existence of traveling ionospheric disturbances (TIDs) on the 24 April 2023 over the African-European region. For this aspect, different regional and global GNSS receiver networks including South Africa's Trignet GPS network, the EUREF Permanent GNSS Network (Bruyninx et al., 2019), International GNSS Service (IGS) network and the EarthScope Consortium have been used.

2.3. TIE-GCM

We have used the first principles, 3-dimensional and self-consistent nonlinear representation of the thermosphere-ionosphere system based on the Thermosphere Ionosphere Electrodynamics General Circulation Model (TIE-GCM) (Qian et al., 2014; Richmond et al., 1992; Roble et al., 1988) to estimate the electron density peaks in the E and F regions and also the O/N_2 column density ratio for the period of 23–24 April 2023. The version of the TIE-GCM used in the study has a horizontal resolution of 1.25° in latitude and longitude, and a vertical resolution of a 1/4 scale height, and it extends from ∼97 km to ∼700 km in altitude. The model simulations were driven by the time-dependent high-latitude plasma convection and auroral precipitation patterns obtained from the Assimilative Mapping of Ionospheric Electrodynamics (AMIE) procedure (e.g., Richmond et al., 1992). The data inputs to AMIE for this event include ground magnetic field perturbations from a worldwide network of 184 magnetometer stations, auroral precipitation inferred from the Special Sensor Ultraviolet Spectrographic Imager onboard the Defense Meteorological Satellite Program (DMSP) spacecraft (e.g., F17 and F18), the cross-track ion drifts from the five DMSP spacecrafts (e.g., F16, F17, and F18), the line-of-sight ion drifts from the Super Dual Auroral Radar Network high frequency radar network, and the magnetic field measurements by the Iridium satellite constellation under the auspice of the Active Magnetospheric and Planetary Electrodynamics Response Experiment project (Anderson et al., 2018). The AMIE patterns have a 5-min time resolution, with a grid size of 1.7° in magnetic latitude (MLAT) and 0.67 hr in magnetic local time (MLT). The AMIE patterns are spatially interpolated to the TIEGCM's grids and temporally interpolated into a 5-s cadence at which the simulation is being performed. The TIEGCM outputs are recorded every 5 min.

3. Results

Figure 4 shows diurnal changes of different frequencies over (a) GR13L and (b) PQ052. Plotted in black, red, blue and magenta colors are ionosonde foF2, monthly median foF2 for April 2023, derived foF2 (based on GPS TEC using equations in Figure 3) and monthly median foE, respectively. In the bottom panels of both Figures 4a and 4b, only foF2 data for 24 April 2023 are plotted over GR13L and PQ052 to clearly show existing data gaps as a result of sample observations shown in Figure 2. For GR13L, data gaps in ionosonde foF2 data can be seen during 0255–0440 UT and 0950–1025 UT. An almost 3 hr duration (0830–1130 UT) data gap can be seen in PQ052 data on 24 April 2023. Based on monthly median foF2, there was a decrease of foF2 over GR13L and PQ052 on 24 April 2023. While there is an overestimation of foF2 (especially over GR13L) based on GPS TEC, the decrease of foF2 is correctly identified by the established linear relationship between NmF2 and TEC.

Overall, we have established that the derived foF2 data during the 23–24 April 2023 were comparable to actual foF2 observations, and thus it may not have been possible that the electron density could have been depleted to significantly low levels not to reflect radio waves in HF band. Otherwise, the derived foF2 will have been lower than monthly median foE and as seen in Figure 4, this is not the case for both GR13L and PQ052. The typical ionospheric plasma frequency is ∼2–20 MHz (HF band) making radio waves within this range to be reflected off the ionosphere, enabling HF communication to be possible (e.g., Hapgood, 2018). Radio waves entering the ionosphere below this plasma frequency range are likely to be attenuated. It should however be emphasized that

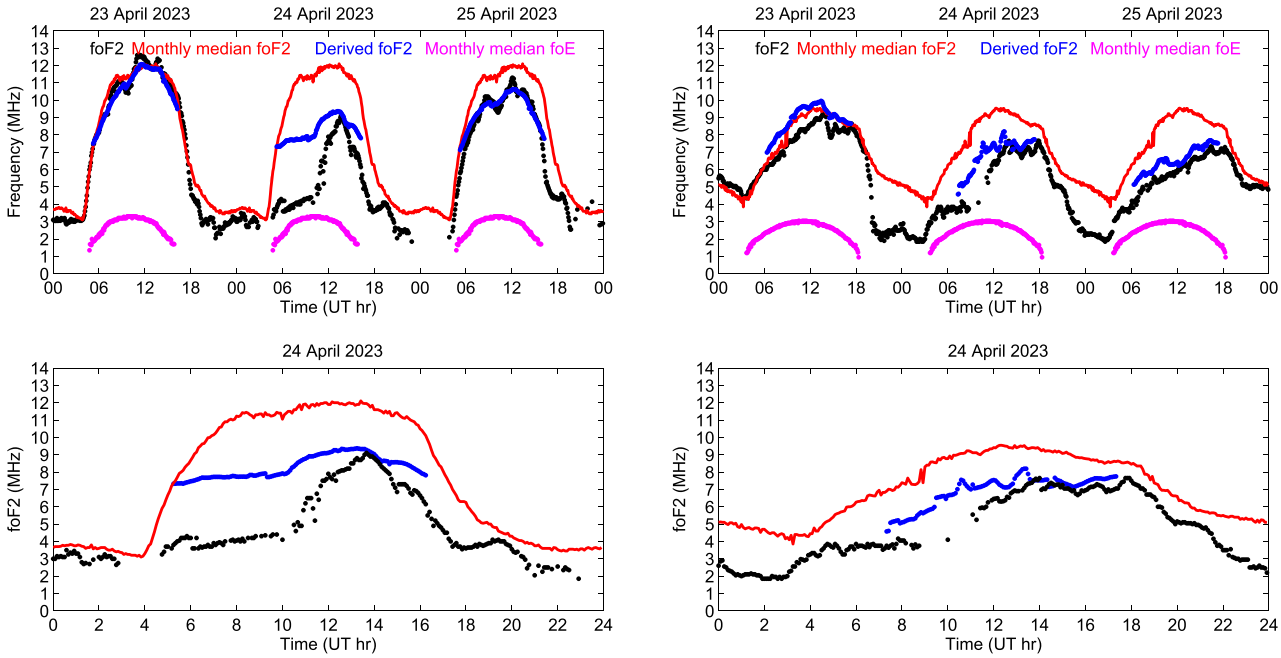

(a) Grahamstown, GR13L (33.3°S, 26.5°E) (b) Pruhonice, PQ052 (50.0°N, 14.6°E)

Figure 4. Variations of measured foF2 (black dots), monthly median foF2 (red curve), derived foF2 (blue dots) and monthly median foE (magenta curve) over (a) Grahamstown and (b) Pruhonice during 23–25 April 2023. The bottom panels of (a) and (b) show foF2, and the respective monthly median values as well derived foF2 for 24 April 2023 to clearly demonstrate data gaps in observations during local daytime.

the plasma frequency depends on electron density which is further influenced by random (geomagnetic and solar activities) and periodic (diurnal and seasonal variations) changes (e.g., McNamara, 1991; Danilov, 2001). Additionally, the ability for sounding the whole ionosphere relies on the instrument's capabilities. In our case, the ionosonde is unable to sound the D region due to low electron densities which do not allow reflection of ionosonde operation frequencies.

An intriguing observation is the simultaneous presence and absence of the E and F layer echoes, respectively. This is especially clear for PQ052 as seen in Figure 2b, on 24 April 2023 at 1005 UT. In absence of actual F2 layer observations during some times, Figure 5 shows maxima electron densities of F2 (NmF2) and E (NmE) layers data from TIE-GCM (e.g., Richmond et al., 1992), Oxygen to Nitrogen (O/N_2) ratio, meridional wind velocity (V_{mer}) at altitude of 250 km for 23–24 April 2023 over GR13L and PQ052 as well as latitudinal changes of V_{mer} (at 250 km altitude) along 15° longitude sector. TIEGCM NmE, NmF2 and O/N_2 data were generated at 5 min intervals. Figure 5b shows that NmE was greater than NmF2 at around 0730–1450 UT over PQ052 which covers the whole duration of F2 layer echoes' absence (0830–1130 UT) during the storm main phase on 24 April 2023. This may be the most likely cause of F2 layer echoes absence over PQ052 during the negative storm phase. Figure 5c shows that O/N_2 ratio decreased on 24 April 2023 in agreement with NmF2 observations with reference to the previous day over both GR13L and PQ052. Thus, similar to NmF2 (foF2) behaviour in Figure 4, TIEGCM results show a decrease in O/N_2 ratio on 24 April 2023. Storm time electron density depletion is mainly linked to thermospheric composition changes (e.g., Fuller-Rowell et al., 1996) which manifest clearly in O/N_2 ratio variability that mainly affect the F2 layer. The E layer is least affected by O/N_2 dynamics because it is dominated by molecular ions and has low O density.

Furthermore, Figure 6 shows the changes in O/N_2 ratio during the 23–25 April 2023 from the Global Ultraviolet Imager (GUVI).

The O/N_2 on 23 April 2023 over South Africa and Europe was not disturbed coinciding with expected normal ionosondes operation as evidenced in the clear ionograms (see right panels of Figure 2). However, there is a

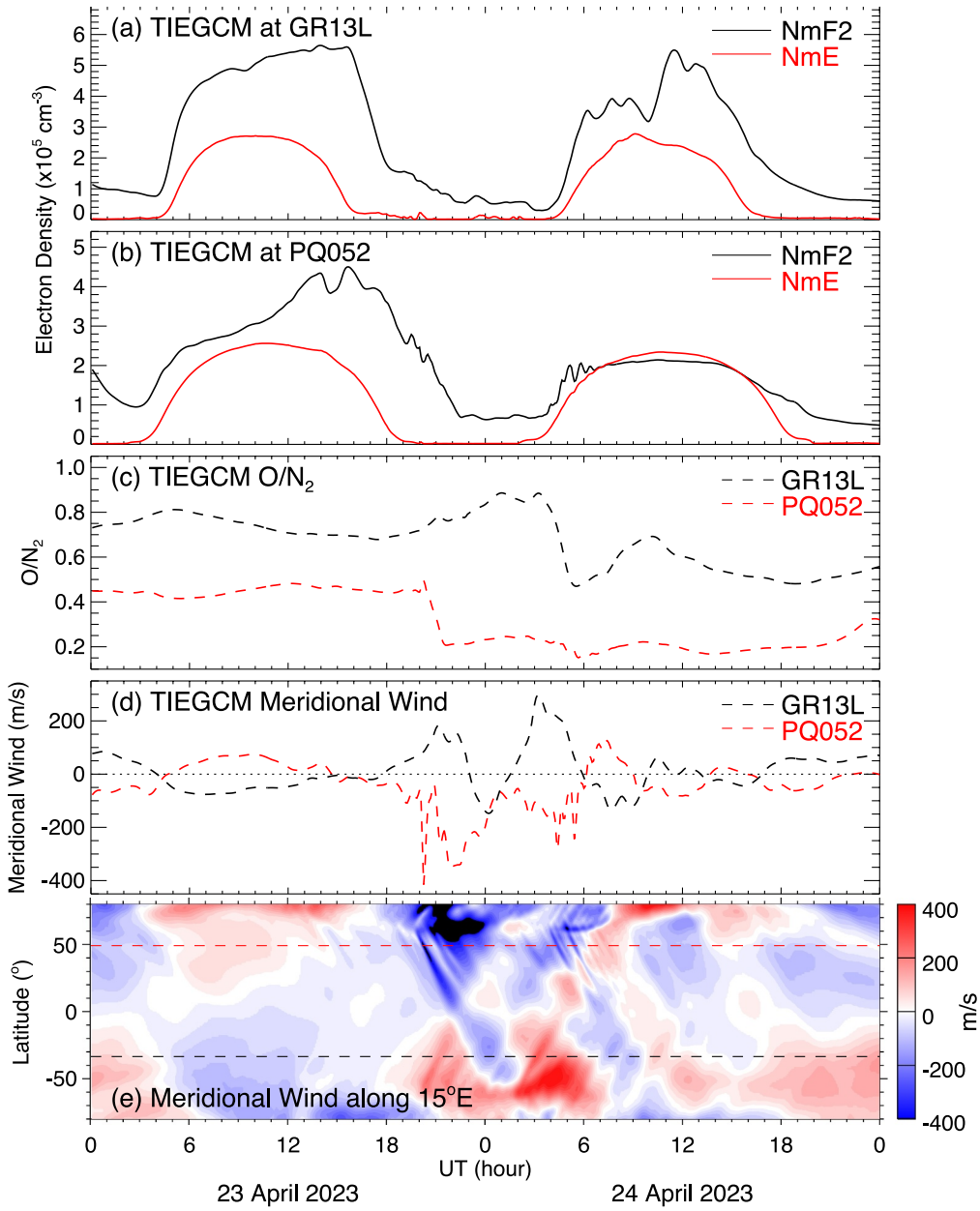

Figure 5. TIE-GCM NmE and NmF2 plotted as red and black solid curves, respectively; and O/N$_2$ ratio for 23–24 April 2023 over GR13L and PQ052. TIEGCM meridional wind at 250 km over GR13L and PQ052 are plotted in panel (d) while panel (e) shows the latitudinal variations of the meridional wind along the 15° longitude sector. The horizontal black and red dashed lines in (e) indicate latitude locations for GR13L and PQ052.

significant O/N$_2$ depletion over Southern Africa at around 1100 local time on 24 April 2023, which is within the time range when F2 layer HF echoes were either absent or faint over both GR13L and PQ052. This indicates a large horizontal gradient in O/N$_2$ ratio and hence NmF2 pointing to a possibly tilted ionosphere. The ionospheric tilting leads to the radio waves to be reflected far away from the ionosonde location resulting into data gaps in foF2 observations as examples show in Figure 4 during 0950–1025 UT and 0830–1130 UT over GR13L and PQ052 respectively. The practical implication of this scenario is that it may have been impossible to use the F2 region for HF communications during this time period. Over time, HF has played a vital role for long distance communication in the African continent within several sectors such as disaster management and relief, aviation and defence/security (e.g., Tshisaphungo et al., 2011). For example, during

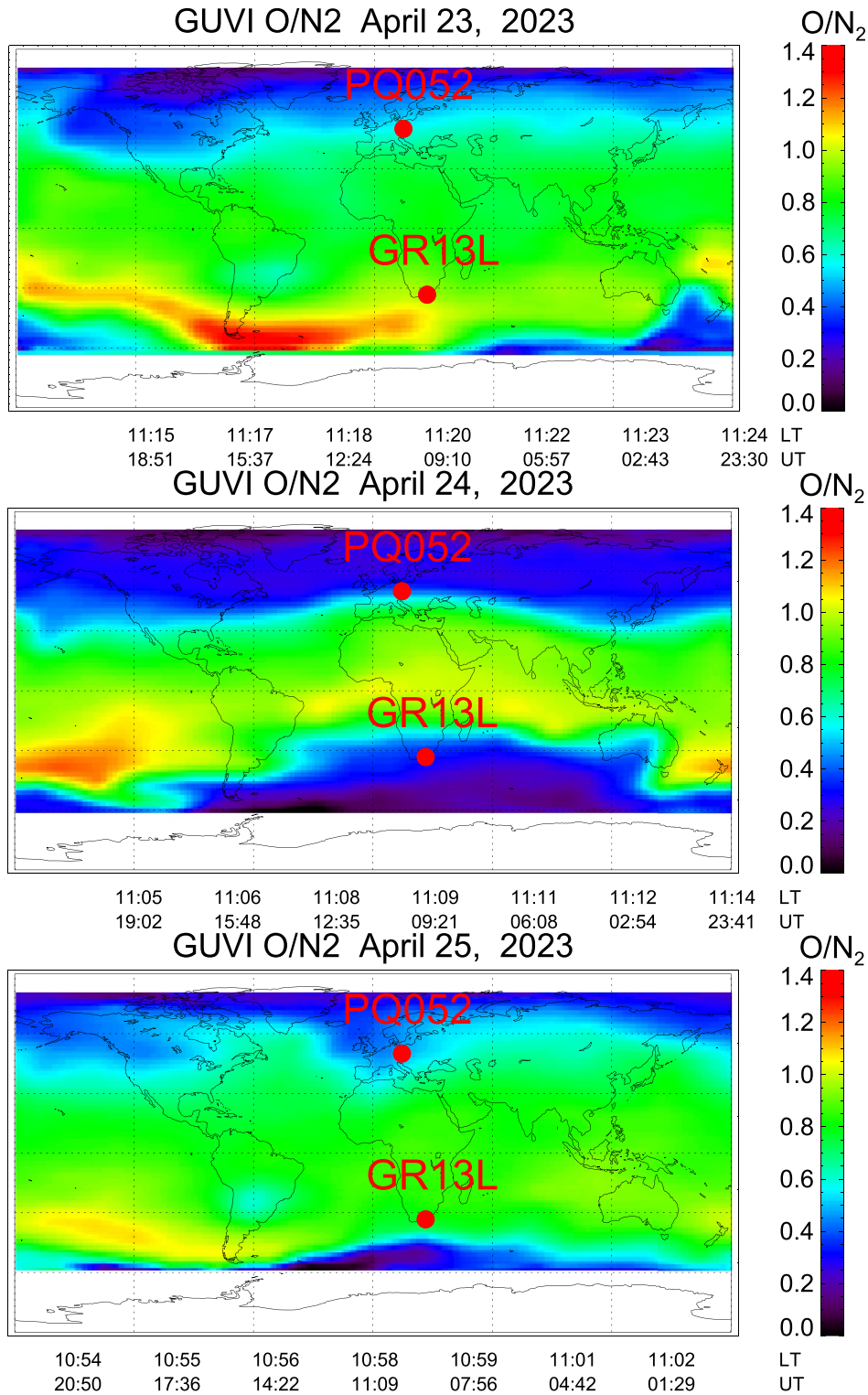

Figure 6. Changes in O/N_2 ratio during 23–25 April 2023. Ionosonde locations PQ052 and GR13L are plotted in red dots.

the extensive damage of communication (internet and telephone) infrastructure and services caused by cyclones in Mozambique, HF communication emerged as the only alternative to coordinate disaster relief efforts (Millership, 2022). Of recent, the need for HF monitoring and forecasting has gained tremendous global

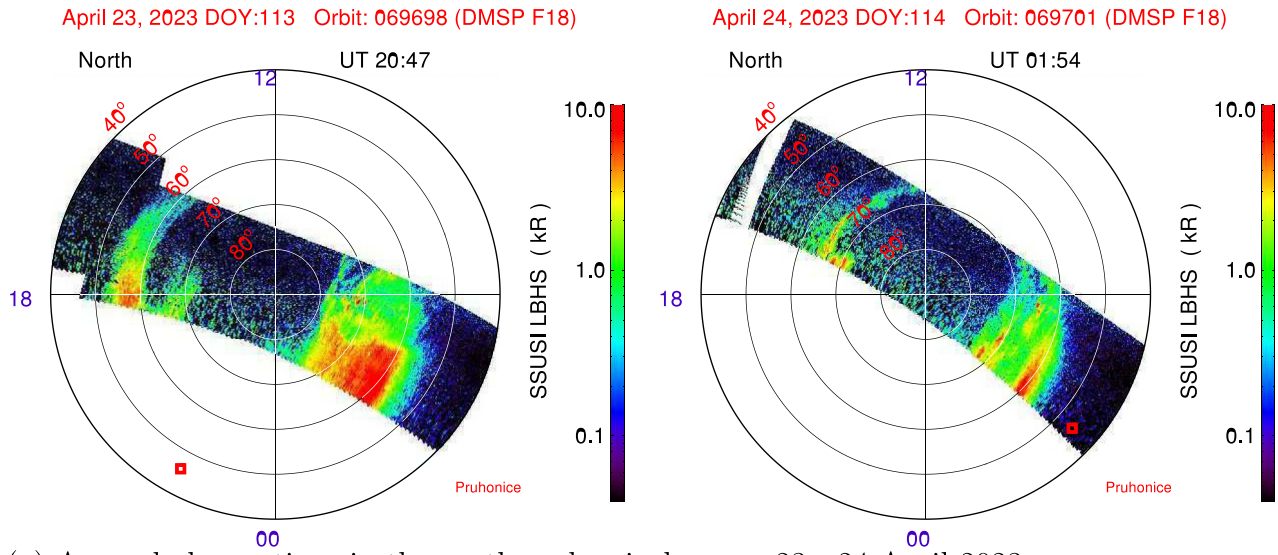

(a) Auroral observations in the northern hemisphere on 23 - 24 April 2023

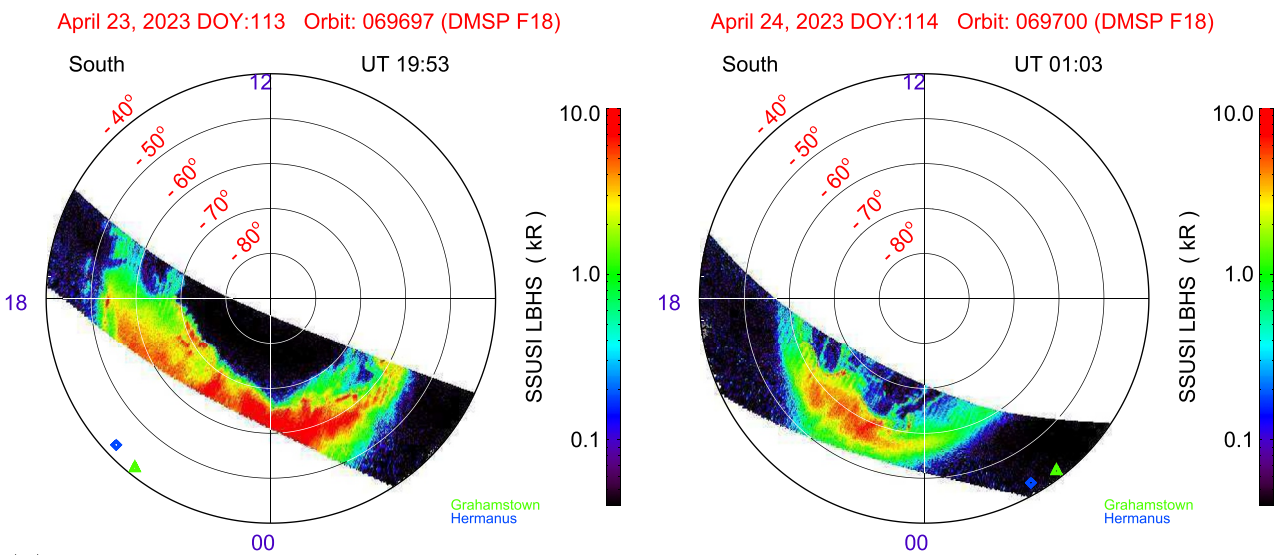

(b) Auroral observations in the southern hemisphere on 23 - 24 April 2023

Figure 7. Auroral observations in (a) northern and (b) southern hemispheres for selected times on 23–24 April 2023 from the Defense Meteorological Satellite Program (DMSP) spacecraft.

attention in response to the International Civil Aviation Organisation (ICAO) recommendation to have access to this form of communication (where possible) for civil aviation purposes (ICAO, 2018, Manual on Space Weather). Compared to the 23 April 2023, Figure 5d shows that the meridional wind velocity reversed from poleward to equatorward direction over both GR13L (~1000–1300 UT) and PQ052 (~0900–1300 UT) on 24 April 2023. Examined along the 15°E longitude sector (Figure 5e), the meridional wind results indicate that the reversal may be a result of storm-time induced equatorward winds which re-distribute the oxygen depleted air (resulting from atmospheric upwelling in auroral regions due to joule heating at high latitudes) from high to mid latitudes leading to reduced electron density (e.g., Burns et al., 1995; Zhang et al., 2004). This result is consistent with both TIEGCM and GUVI O/N_2 observations on 24 April 2023 over both GR13L and PQ052. Pre-storm and storm time zonal winds (not shown) do not show any significant differences during the 23 and 24 April 2023, respectively.

4. Discussion

Absence of HF signals from the ionosphere as measured by ionosondes is well known to be associated with flare activity (e.g., Mitra, 1974; Yasyukevich et al., 2018). However, there were no solar flares on 24 April 2023 that may have affected the ionosphere to the extent of absorbing HF radio waves. The observed negative storm effect on 24 April 2023 was due to the changes in thermospheric composition (e.g., Fuller-Rowell et al., 1994, 1996) as confirmed by the GUVI O/N_2 ratio data (Zhang et al., 2004) and TIEGCM simulation results. The NmF2 depletion process emanates from the joule heating that leads to atmospheric upwelling in the auroral region. During the redistribution of the oxygen depleted air from the lower thermosphere to F region by neutral winds, the auroral oval can extend from high to midlatitudes (e.g., Fuller-Rowell et al., 1996; Prölss, 1980; Zhang et al., 2004). This scenario is supported by auroral oval activity results during the geomagnetic storm of 23–25 April 2023. Figure 7 shows the position of equatorward auroral oval on 23–24 April 2023 with locations of GR13L (~42°S, magnetic) and PQ052 (~46°N, magnetic) marked in red square and green triangles, respectively. Auroral oval information are provided by the Special Sensor Ultraviolet Spectrographic Imager (SSUSI) on board the Defense Meteorological Satellite Program (DMSP) F18 space craft. Plotted is the intensity of the aurora observations in the Lyman-Birge-Hopfield Shortband, LBHS wavelength corresponding to 140–150 nm.

The images in Figure 7 are mapped to magnetic latitude - local time frame where dawn and dusk sides appear on the right and left, respectively; with mid-night at the bottom. Over the southern hemisphere, Hermanus, HE13N (34.4°S, 19.2°E) is also indicated in blue square. HE13N and GR13L have almost similar MLAT (~42°S) with a local time difference of about 30 min. Quiet time equatorward auroral oval boundary (EAB) is usually constrained within 70°–80° magnetic latitude (MLAT), although it exhibits morning-evening and day-night asymmetry (e.g., Xiong et al., 2014). Statistically, the EAB may extend below 60° MLAT during disturbed conditions, Kp > 4 (Xiong et al., 2014). After the SSC on 23 April 2023, Kp reached a value of 8 between 1800 and 2100 UT, and results in Figure 7 show that the EAB expanded beyond 60° MLAT towards midlatitudes in both northern and southern hemispheres. Thus, the DMSP/SUSSI F18 results on 23 (after the SSC) and 24 April 2023 indicate that the auroral oval was closer to both Europe and South Africa. This suggests that high latitude Joule and particle heating extended to latitude well below 60° magnetic latitude and created O/N_2 depletion in the Europe and South Africa sectors, consistent with the observed foF2 depletions. It is interesting to note that storm-time O/N_2 depletion observed by TIMED/GUVI usually does not reach South Africa.

To investigate the possible role played by horizontal gradients in electron density, Figure 8 shows an example of the TEC spatial gradient maps over South Africa. The maps cover a 15 min period from 1120 UT to 1135 UT (in 5 min intervals). This is a period when there were unclear or faint F2 echoes over GR13L. The TEC spatial gradient maps are generated using the Scharr operator (Scharr, 2007) and have resolution of 1° × 1° latitude/longitude. Further details on the comprehensive procedure of generating these gradient maps can be found in Matamba and Danskin (2022). An essential component of the gradient maps is the gridding of TEC at ionospheric pierce points in 1° × 1° latitude/longitude followed by median filtering in each bin to eliminate potential errorneous data. The location of GR13L is 33.3°S and 26.5°E latitude/longitude clearly positions it within the area of steep spatial plasma gradient during this time interval. We observe TEC gradients exceeding 0.7 TECU/degree which are considered significant. According to Matamba and Danskin (2022), insignificant TEC gradients are less than 0.5 TECU/degree. The steep TEC gradients are not clear during 0255–0440 UT, presumably because the plasmasphere is the major contributor of electron content during local nighttime reaching over 40%–60% (e.g., Habarulema et al., 2021; Yizengaw et al., 2008), and yet it is suggested that such gradients were located within the ionosphere. Steep electron density gradients in midlatitudes have been observed, for example, during the geomagnetic storm of 11–12 April 2001 (Park et al., 2012). However these observations are different from our results as the midlatitude gradients for 11–12 April 2001 storm occurred during strong density enhancements and were associated with corotation time of the noon sector plasma density enhancement (Park et al., 2012). The steep plasma gradients of 24 April 2023 occurred within a depleted ionospheric electron density environment that is directly linked to changes in thermospheric composition as evidenced in extension of the depleted O/N_2 ratio to mid latitude regions. The source of the plasma density gradients is related to O/N_2 ratio dynamics and expansion of EAB towards mid-latitudes during the storm main phase. Finally, Figure 9a shows GUVI and TIEGCM O/N_2 ratio at 1049 LT (~0903 UT and 0951 UT over GR13L and PQ052, respectively). Both TIMED/GUVI and TIEGCM O/N_2 show a clear spatial gradient in the O/N_2 depleted regions, suggesting F-region ionosphere was tilted. Figure 9b represents TEC perturbations (ΔTEC) over the African-European sector within longitude and latitude ranges of 20–40°E and 40°S–70°N, respectively. ΔTEC data are derived from the difference between

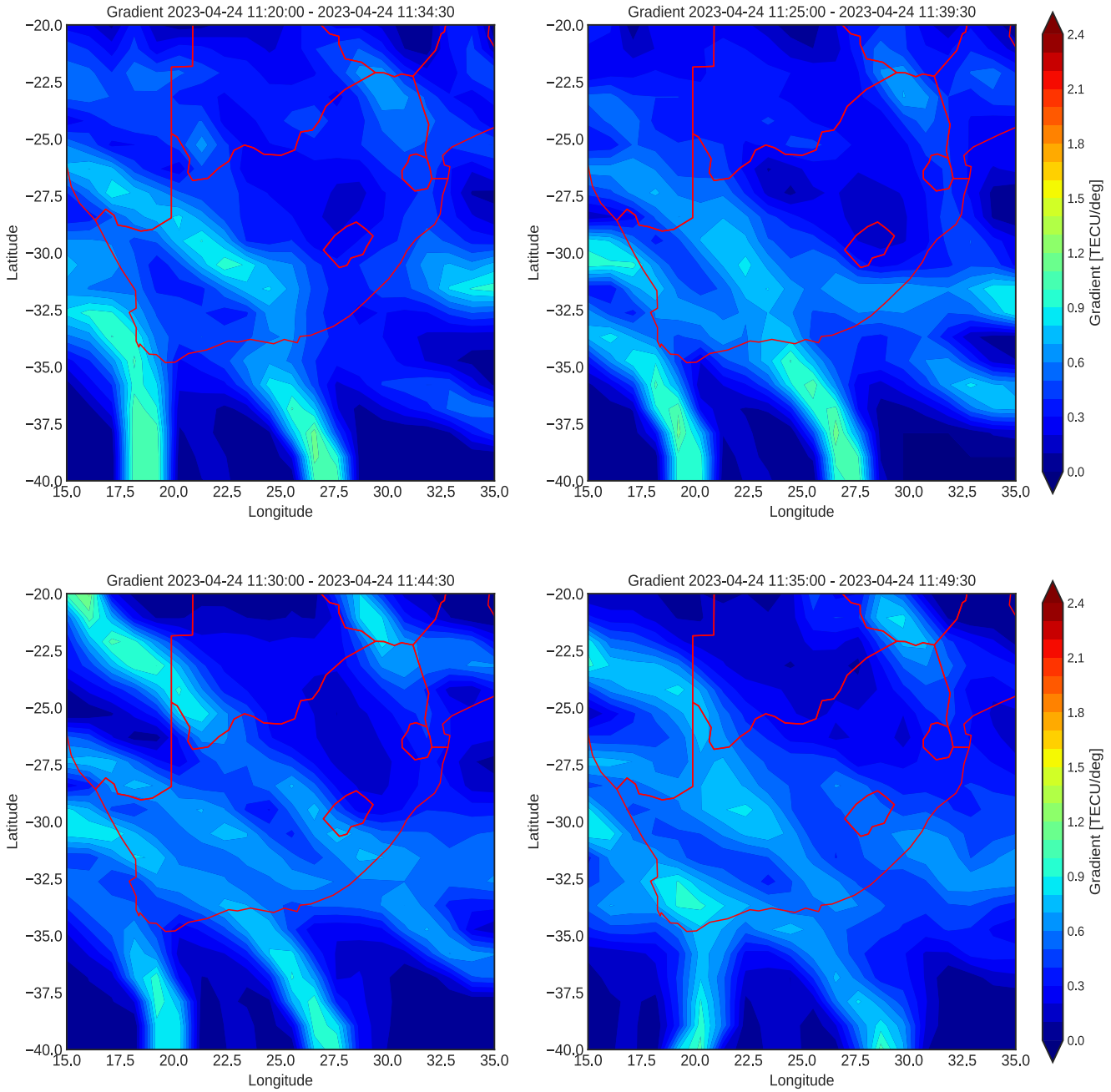

Figure 8. TEC gradient maps over Southern Africa on 24 April 2023 during 1120–1135 UT.

each PRN's TEC and the corresponding fitted TEC values using a fourth order polynomial. Thereafter we bin ΔTEC data in 2° latitude and 3 min and plot median in each bin as shown in Figure 9b. Median ΔTEC values are preferable over mean in each bin to avoid dealing with extremely high ΔTEC (e.g., Habarulema et al., 2022). The solid gray horizontal lines indicate latitudes of GR13L (33.3°S) and PQ052 (50.0°N) during 0900–1140 UT and 0830–1130 UT when F2 region echoes were either faint or absent. Over the southern hemisphere, we observe equatorward TID activity which may be related to storm-time processes in high latitudes such as Joule heating (Danilov, 2001; Prölss, 1980) during the period of absent and faint F2 region echoes. The presence of unclearly defined F2 echoes may be due to both low F2 layer density and ionospheric tilt. The tilt could be due to back ground density gradient and/or passing of TIDs (Paznukhov et al., 2020).

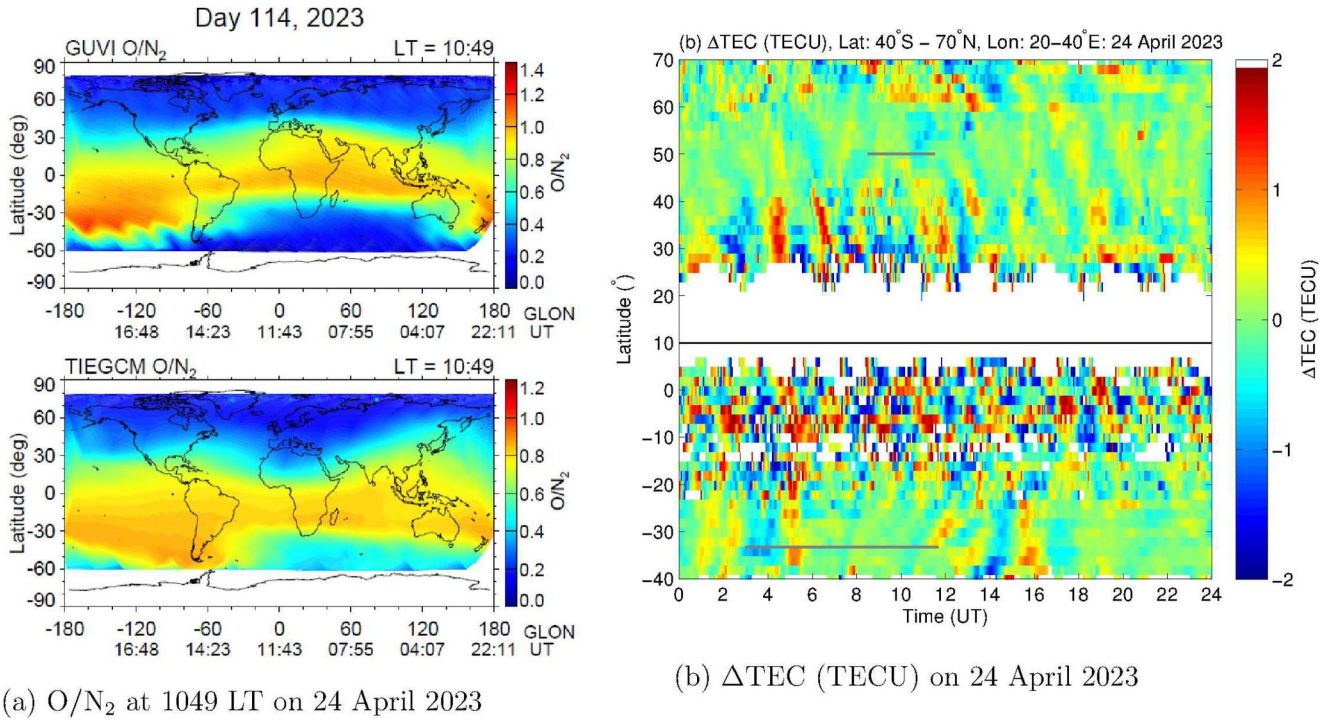

(a) O/N_2 at 1049 LT on 24 April 2023

(b) ΔTEC (TECU) on 24 April 2023

Figure 9. (a) GUVI and TIEGCM O/N_2 ratio at 1049 LT, and (b) ΔTEC (TECU) over the Africa-European longitude sector (20–40°E) on 24 April 2023.

5. Conclusions

This paper has investigated the ionospheric storm response during the geomagnetic storm period of 23–25 April 2023. Of particular interest was the absence of (or extremely faint) HF echoes (particularly from the F2 layer) as seen from ionosonde data on 24 April 2023 over PQ052 and GR13L, both mid latitude locations in Czech Republic and South Africa, respectively. With changes in O/N_2 ratio which showed depletions reaching mid latitudes and TEC observations over Southern Africa revealing plasma density gradients, we link absence of HF echoes to possible ionospheric tilting during the main phase of the storm on 24 April 2023 especially over the southern hemisphere's GR13L. Simulation results from TIEGCM (Richmond et al., 1992) revealed that NmE was greater than NmF2 over PQ052 during the period when there were no F2 layer echoes while at the same time the E layer was clear in ionograms. This made it impossible to receive F region echoes as only lower frequencies were reflected from the E region.

Data Availability Statement

Ionosonde data can be obtained from www.sansa.org.za and https://giro.uml.edu/. The GNSS observations are provided by the University Navstar Consortium, UNAVCO (https://www.unavco.org/data/gps-gnss/gps-gnss.html and ftp://data-out.unavco.org), the EUREF Permanent GNSS Network (https://www.epncb.eu/pub/obs/2023/114/ and ftp://ftp.epncb.oma.be/pub/obs/2023/114/) and South African National Geospatial Information (www.trignet.co.za and ftp://ftp.trignet.co.za). Solar wind parameters were obtained from https://spdf.gsfc.nasa.gov/pub/data/omni/high_res_omni/. SYM-H data were downloaded from https://omniweb.gsfc.nasa.gov/form/dx1.html. TIMED/GUVI O/N_2 data were downloaded from http://guvitimed.jhuapl.edu/data_fetch_l3_on2_netcdf. DMSP SSUSI auroral data are from https://ssusi.jhuapl.edu/data_availability?spc=f16&type=edr-aur.

Acknowledgments
This work is based on the research supported in part by the National Research Foundation of South Africa (Grants 116005, 129285, and TTK2204072545) and opinions, findings and conclusions or recommendations expressed in this paper are of the author(s), and the NRF accepts no liability whatsoever in this regard. YZ is partially supported by NASA Grants 80NSSC20K0354 and 80NSSC21K1673.

References

Anderson, B. J., Olson, C. N., Korth, H., Barnes, R. J., Waters, C. L., & Vines, S. K. (2018). Temporal and spatial development of global Birkeland currents. *Journal of Geophysical Research: Space Physics*, *123*(6), 4785–4808. https://doi.org/10.1029/2018ja025254

Blanc, M., & Richmond, A. D. (1980). The ionospheric disturbance dynamo. *Journal of Geophysical Research*, *85*(A4), 1669–1686. https://doi.org/10.1029/ja085ia04p01669

Bruyninx, C., Legrand, J., Fabian, A., & Pottiaux, E. (2019). GNSS metadata and data validation in the EUREF Permanent Network. *GPS Solutions*, *23*(106), 106. https://doi.org/10.1007/s10291-019-0880-9

Burns, A. G., Killeen, T., Carignan, G., & Roble, R. (1995). Large enhancements in the O/N_2 ratio in the evening sector of the winter hemisphere during geomagnetic storms. *Journal of Geophysical Research*, *100*(A8), 14661–14671. https://doi.org/10.1029/94ja03235

Danilov, A. D. (2001). F2-region response to geomagnetic disturbances. *Journal of Atmospheric and Solar-Terrestrial Physics*, *63*(5), 441–449. https://doi.org/10.1016/s1364-6826(00)00175-9

Fagundes, P. R., Pezzopane, M., Habarulema, J. B., Venkatesh, K., Dias, M. A. L., Tardelli, A., et al. (2020). Ionospheric disturbances in a large area of the terrestrial globe by two strong solar flares of September 6, 2017, the strongest space weather events in the last decade. *Advances in Space Research*, *66*(7), 1775–1791. https://doi.org/10.1016/j.asr.2020.06.032

Fuller-Rowell, T. J., Codrescu, M. V., Moffett, H. R. R. J., Quegan, R. J., & Quegan, S. (1996). On the seasonal response of the thermosphere and ionosphere to geomagnetic storms. *Journal of Geophysical Research*, *101*(A2), 2343–2353. https://doi.org/10.1029/95ja01614

Fuller-Rowell, T. J., Codrescu, M. V., Moffett, R. J., & Quegan, R. J. (1994). Response of the thermosphere and ionosphere to geomagnetic storms. *Journal of Geophysical Research*, *99*(A3), 3893–3914. https://doi.org/10.1029/93ja02015

Ghag, K., Raghav, A., Bhaskar, A., Soni, S., Sathe, B., Shaikh, Z., et al. (2023). ICME pancaking: A cause of two-step severe storm ($Dst \approx -187$ nT) of 25th solar cycle observed on 23 April 2023. preprint, arXiv.2305.05381v1.

Habarulema, J. B., Okoh, D., Bergeot, N., Buresova, D., Matamba, T., Tshisaphungo, M., et al. (2021). Interhemispheric comparison of the ionosphere and plasmasphere total electron content using GPS, radio occultation and ionosonde observations. *Advances in Space Research*, *68*(6), 2339–2353. https://doi.org/10.1016/j.asr.2021.05.004

Habarulema, J. B., Tshisaphungo, M., Katamzi-Joseph, Z. T., Matamba, T. M., & Nndanganeni, R. (2022). Ionospheric response to the M- and X-class solar flares of 28 October 2021 over the African sector. *Space Weather*, *20*(8), e2022SW003104. https://doi.org/10.1029/2022SW003104

Hapgood, M. (2018). Linking space weather science to impacts - The view from the Earth. In *Chapter 1: In extreme events in geospace; origins, predictability and consequences* (pp. 3–34). https://doi.org/10.1016/B978-0-12-812700-1.00001-7

Huang, C. S. (2012). Statistical analysis of dayside equatorial ionospheric electric fields and electrojet currents produced by magnetospheric substorms during sawtooth events. *Journal of Geophysical Research*, *117*, A02316. https://doi.org/10.1029/2011JA017398

ICAO. (2018). Manual on space weather information in support of international air navigation (1st ed.). Doc 10100.

Kouris, S. S., Xenos, T. D., Polimeris, T. D., & Stergiou, D. (2004). TEC and foF2 variations: Preliminary results. *Annals of Geophysics*, *47*(4), 1325–1332.

Matamba, T. M., & Danskin, D. W. (2022). Development and evaluation of near-real time TEC and ancillary products for SANSA Space Weather. *Space Weather*, *20*(5), e2021SW003013. https://doi.org/10.1029/2021sw003013

McNamara, L. F. (1991). The ionosphere: Communications. *Surveillance and direction finding*. Krieger Publishing Company.

Millership, E. (2022). Tuning into 'amateur' radio airwaves in Mozambique. Retrieved from https://www.wfp.org/stories/tuning-amateur-radio-airwaves-mozambique

Mitra, A. P. (1974). *Ionospheric effects of solar flares*. D. Reidel Publishing Company.

Park, S., Kim, K.-H., Kil, H., Jee, G., Lee, D.-H., & Goldstein, J. (2012). The source of the plasma density gradient in middle latitudes during the 11-12 April 2001 storm. *Journal of Geophysical Research*, *117*(A05313), 1131–1164. https://doi.org/10.1029/2011JA017349

Paznukhov, V., Altadill, D., Juan, J. M., & Blanch, E. (2020). Ionospheric tilt measurements: Application to traveling ionospheric disturbances climatology study. *Radio Science*, *55*(2), e2019RS007012. https://doi.org/10.1029/2019RS007012

Pignalberi, A., Habarulema, J. B., Pezzopane, M., & Rizzi, R. (2019). On the development of a method for updating an empirical climatological ionospheric model by means of assimilated vTEC measurements from a GNSS receiver network. *Space Weather*, *17*(7), 1131–1164. https://doi.org/10.1029/2019SW002185

Prölss, G. W. (1980). Magnetic storm associated perturbations of the upper atmosphere: Recent results obtained by satellite-borne gas analyzers. *Reviews of Geophysics*, *18*(1), 183–202. https://doi.org/10.1029/rg018i001p00183

Prölss, G. W., & Jung, M. (1978). Travelling atmospheric disturbances as a possible explanation for daytime positive storm effects of moderate duration at middle latitudes. *Journal of Atmospheric and Terrestrial Physics*, *40*(12), 1351–1354. https://doi.org/10.1016/0021-9169(78)90088-0

Qian, L., Burns, A. G., Emery, B. A., Foster, B., Lu, G., Maute, A., et al. (2014). The NCAR TIE-GCM. In J. Huba, R. Schunk, & G. Khazanov (Eds.), *Modeling the ionosphere-thermosphere system*. https://doi.org/10.1002/9781118704417.ch7

Richmond, A. D., Ridley, E. C., & Roble, R. G. (1992). A thermosphere/ionosphere general circulation model with coupled electrodynamics. *Geophysical Research Letters*, *19*(6), 601–604. https://doi.org/10.1029/92GL00401

Roble, R. G., Ridley, E. C., Richmond, A. D., & Dickinson, R. E. (1988). A coupled thermosphere/ionosphere general circulation model. *Geophysical Research Letters*, *15*(12), 1325–1328. https://doi.org/10.1029/gl015i012p01325

Scharr, H. (2007). Optimal filters for extended optical flow. In *Lecture notes in computer science* (Vol. 3417). Springer. https://doi.org/10.1007/978-3-540-69866-1-2

Seemala, G. K. (2023). Estimation of ionospheric total electron content (TEC) from GNSS observations. In *Chapter 4 in atmospheric remote sensing principles and applications*. Elsevier.

Ssessanga, N., McKinnell, L. A., & Habarulema, J. B. (2014). Estimation of foF2 from GPS TEC over the South African region. *Geophysical Research Letters*, *112*, 20–30. https://doi.org/10.1016/j.jastp.2014.02.003

Tshisaphungo, M., McKinnell, L. A., Magnus, L., & Habarulema, J. B. (2011). An attempt to validate HF propagation prediction conditions over Sub-Saharan Africa. *Space Weather*, *9*(8), S08001. https://doi.org/10.1029/2010SW000643

Tsurutani, B., Mannucci, A., Iijima, B., Abdu, M. A., Sobral, J. H. A., Gonzalez, W., et al. (2004). Global dayside ionospheric uplift and enhancement associated with interplanetary electric fields. *Journal of Geophysical Research*, *109*(A8), A08302. https://doi.org/10.1029/2003JA010342

Xiong, C., Lühr, H., Wang, H., & Johnsen, M. G. (2014). Determining the boundaries of the auroral oval from CHAMP field-aligned current signatures - Part 1. *Annals of Geophysics*, *32*(6), 609–622. https://doi.org/10.5194/angeo-32-609-2014

Yasyukevich, Y., Astafyeva, E., Padokhin, A., Ivanova, V., Syrovatskii, S., & Podlesnyi, A. (2018). The 6 September 2017 X-class solar flares and their impacts on the ionosphere, GNSS, and HF radio wave propagation. *Space Weather*, *16*(8), 1013–1027. https://doi.org/10.1029/2018SW001932

Yizengaw, E., Moldwin, M. B., Galvan, D., Iijima, B. A., Komjathy, A., & Mannucci, A. J. (2008). Global plasmaspheric TEC and its relative contribution to GPS TEC. *Journal of Atmospheric and Solar-Terrestrial Physics*, *70*(11–12), 1541–1548. https://doi.org/10.1016/j.jastp.2008.04.022

Zhang, Y., Paxton, L. J., Morrison, D., Wolven, B., Kil, H., Meng, C.-I., et al. (2004). O/N_2 changes during 1–4 October 2002 storms: IMAGE SI-13 and TIMED/GUVI observations. *Journal of Geophysical Research*, *109*(A10), A10308. https://doi.org/10.1029/2004JA010441